NOSETIP ROUGHNESS AND SPECTRAL ANALYSIS OF HYPERSONIC BOUNDARY LAYER TRANSITION REVERSAL

Andrew P. Ceruzzi, Laurent M. Le Page, Liam P. McQuellin, and Matthew McGilvray

Department of Engineering Science, University of Oxford, Oxford, United Kingdom, OX2 0ES

ABSTRACT

Boundary layer transition on a 7-degree half-angle cone at zero angle of attack with varying bluntness is experimentally investigated in cold Mach 6 flow produced by the High Density Tunnel (HDT) at the University of Oxford. The bluntness Reynolds number, Re_{RN}, defined using freestream conditions and the nose radius, is varied over the range 3×10^4 to 1.5×10^6. The transition Reynolds number, Re_{XST}, increases with Re_{RN} up to approximately $Re_{RN} = 8 \times 10^5$. Beyond this value, Re_{XST} exhibits greater variance and a reversal trend with increasing bluntness, consistent with earlier findings by Stetson [1] and Marineau [2].

The boundary and entropy layers are studied simultaneously using high-speed schlieren imaging at 500 kHz. Schlieren images are analysed using a range of spectral techniques, including spectral proper orthogonal decomposition (SPOD) and continuous wavelet transforms (CWT). Coherent waves in the boundary and entropy layers are identified, with dominant frequency peaks ranging from 20 kHz to above 160 kHz. This analysis provides further data on the instabilities and flow structures that may constitute the mechanisms and pathways leading to boundary transition reversal under these conditions.

Index Terms— Boundary Layer Transition, Spectral Analysis, Hypersonic Flow

1. INTRODUCTION

Predicting the transition of hypersonic boundary layers is of significant interest due to its impact on aerodynamic heating and vehicle performance [3]. The transition from laminar to turbulent flow in high-speed regimes leads to increased skin friction and surface heat flux, affecting both thermal protection system design and overall vehicle efficiency [4, 5]. In recent years, considerable effort has been devoted to understanding the influence of leading-edge bluntness on hypersonic boundary layer stability, particularly in relation to the transition reversal phenomenon [6, 7, 8, 9, 10, 11].

Previous work by Ceruzzi et al. [12] investigated the boundary layer transition on a 7-degree half-angle cone at Mach 6, examining variations in transition location with changes in nose tip bluntness. The study demonstrated that the transition Reynolds number, Re_{XST}, increased with the bluntness Reynolds number, Re_{RN}, up to $\sim 6 \times 10^5$, beyond which transition location became scattered. This behaviour was attributed to transition reversal caused by small roughness on the nose interacting with the very thin boundary layer, as was proposed by Stetson [1]. However, the nosetip roughness was not comprehensively characterized and additionally, the role of flow structures and instability mechanisms in the transition reversal process remains an open question.

This work extends previous investigation by including surface scans of the nosetips, estimation of the nosetip boundary layer properties, and spectral anaylsis of schlieren data. For details concerning the determination of transition onset locations via heat flux measured from infrared (IR) thermography, the reader is referred to Ceruzzi et al. [12].

Spectral analysis techniques, including spectral proper orthogonal decomposition (SPOD) and continuous wavelet transforms (CWT), are applied to the schlieren datasets to characterise boundary layer instabilities and wave interactions [2, 13]. These analyses aim to clarify the mechanisms associated with transition and to assess the relative influence of non-modal growth phenomena and roughness-induced disturbances [7, 6].

2. EXPERIMENTAL ARRANGEMENT

The experiments were carried out in the High Density Tunnel (HDT) at the University of Oxford, a heated Ludwieg tube facility designed for hypersonic aerodynamics studies [14]. This section details the test facility, model configuration, and diagnostic techniques used in the study.

2.1. Flow Facility and Conditions

The HDT consists of a heated Ludwieg tube with a diameter of 152 mm and a total length of 17.35 m, capable of operating at pressures up to 275 bar and total temperatures up to 550 K [15]. The facility was equipped with a Mach 6 nozzle which generates a Mach 6.1 hypersonic flow with a core diameter of 300 mm, allowing boundary layer transition studies under controlled conditions.

The freestream conditions are determined from the total pressure (P_0) and temperature (T_0) measured in the nozzle

plenum with a Kultite XCQ-080 pressure transducer and an aspirated thermocouple, respectively [16, 17]. The freestream Mach number (M_∞) is determined from Pitot pressure measurements taken during Pitot rake surveys conducted prior to the experiments. Freestream pressure (P_∞) and temperature (T_∞) are calculated using isentropic relations, and unit Reynolds numbers are found from the freestream conditions using the viscosity model from Keyes [18]. The facility provided 5 steady-state flow periods per run with each period lasting approximately 40 ms with repeatability ensured through pre-shot Pitot rake surveys.

Freestream turbulence levels were characterised previously using Pitot pressure surveys [19] and Focused Laser Differential Interferometry (FLDI) [20].

A total of 22 tunnel shots were conducted, covering a range of Reynolds numbers and nose radii. A summary of key test conditions and nose radii is provided in Table 1.

Table 1. Summary of test conditions in the experiment.

Condition (-)	P_0 (MPa)	T_0 (K)	M_∞ (-)	Re_∞ (10^6/m)	R_N (mm)
A	1.3	439	6.16	12	3
B	1.9	442	6.16	17	9
C	3.0	440	6.15	27	9
D	3.8	441	6.16	33	15
E	6.4	438	6.16	57	15
F	6.4	455	6.09	55	20
G	6.4	452	6.09	56	25

2.2. Test Model

The test article was a 7° half-angle (θ_c) cone constructed from aluminium alloy with an interchangeable nose tip, allowing variation in nose radius (R_N). The model had a base radius (R_B) of 82.5 mm and was aligned with the centreline of the facility at zero angle of attack and yaw. Nose tips of $R_N = 3, 9, 15, 20$ and 25 mm were used to systematically investigate the effects of bluntness on the location of the transition. A polyether ether ketone (PEEK) insert, 437 mm long, 20 mm wide, and 12 mm deep was integrated into the model to provide a high-emissivity surface for surface heat flux determination via infrared thermography. A schematic of the test model is shown in Figure 1 which details the models geometric parameters, coordinate system and measurement locations.

The alignment of the model was verified using three Kulite XTEL-140(M) pressure transducers positioned 15 mm upstream of the cone shoulder. The mean surface pressure across the transducers was required to remain within 2% of each other to ensure an accurate zero-degree angle of attack and yaw configuration.

2.3. Schlieren Imaging

Schlieren imaging was used to visualise density gradients in the boundary and entropy layers. A Z-type schlieren arrangement with a Cavitar C013 v1.0 Cavilux Smart UHS pulsed laser with 10 ns pulse-width and a Phantom TMX 7510 high-speed camera was used to capture 3000 frames at 500,000 frames-per-second. The knife-edge was aligned to resolve the wall-normal density gradient, $\partial\rho/\partial Y_s$.

3. RESULTS

3.1. Transition Reynolds Numbers

Transition Reynolds numbers were determined using the freestream unit Reynolds number and the measured start of transition location, X_{ST}, which is defined as the streamwise location where the heat flux rises 40% above the laminar heat flux determined using Lee's correlation [21, 22]. These values were originally reported by Ceruzzi et al. [12], and are re-plotted here to more clearly illustrate the influence of nose radius (and associated surface roughness) on the transition Reynolds number, Re_{XST}.

Figure 2 presents the variation of Re_{XST} with bluntness Reynolds number, Re_{RN}. These are plotted with comparative data points from Stetson's experiments [1] (black crosses) which were taken from Figure 8 of Jewel and Kimmel [6], who re-plotted Stetson's data to more clearly illustrate the transition reversal trend.

Figure 3 presents a zoomed-in version of Figure 2 to highlight the differences in behavior with nose radius. A transition reversal trend was observed for the 15 and 25 mm nosetip, while no reversal trend was observed for the 20 mm nosetip. The highlighted red points correspond to conditions in table 1. Conditions A-D are used in the spectral analysis of the flow features observed with schlieren. Conditions E and G correspond to critical Reynolds numbers of transition reversal for the 15 and 25 mm nosetip, respectively. Condition F corresponds to the largest Reynolds number run for the 20 mm nosetip.

3.2. Surface Roughness Characterisation

The surface condition of the nose geometries was assessed using an Alicona InfiniteFocus optical profilometer. This instrument scans the surface along a defined area, recording local height variations with 400 nm resolution. For each nosetip, four scans were taken at 90 degree azimuthal increments, located approximately 45 degrees streamwise from the stagnation point to capture roughness near the sonic point of the nose and to assess azimuthal uniformity. All three nosetips were machined using a CNC lathe with no subsequent surface treatment or polishing. As such, the roughness measurements presented here reflect the intrinsic surface finish produced by that shared machining method.

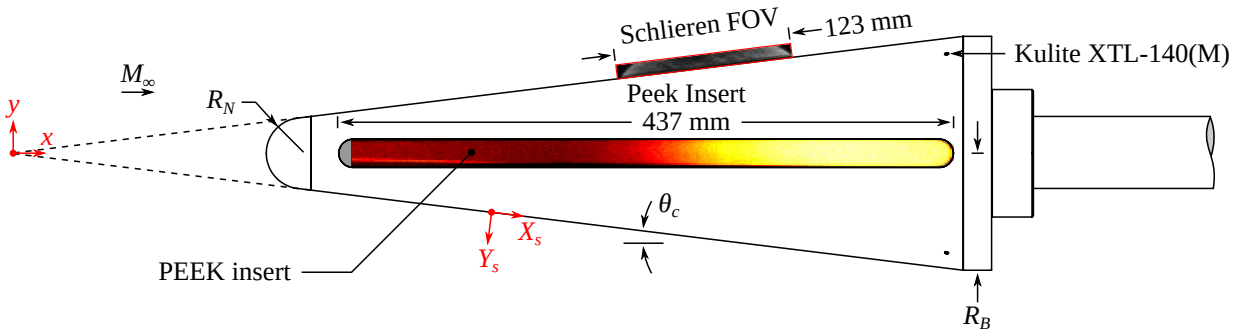

Fig. 1. Schematic of the 7-degree half-angle cone model with interchangeable nose tip.

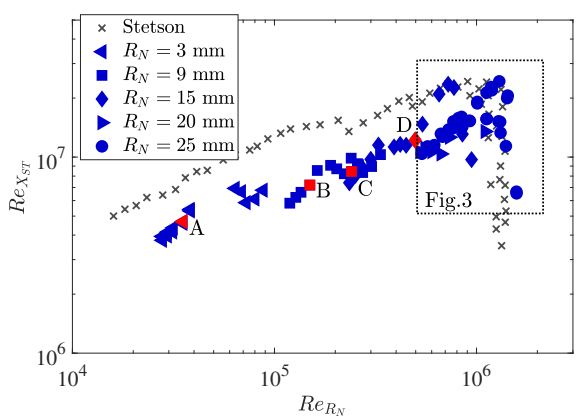

Fig. 2. Transition Reynolds number vs bluntness Reynolds number.

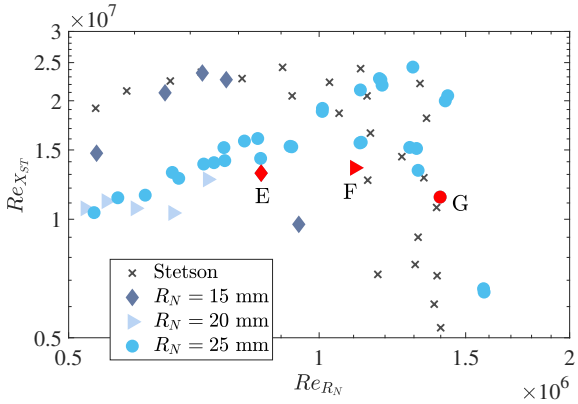

Fig. 3. Transition Reynolds number vs bluntness Reynolds number in the reversal regime.

The $R_N = 20$ & 25 mm nosetips were machined around the same date while the final version of the $R_N = 15$ mm nosetip was re-machined at a later date, after a defect was discovered in the initial version.

A sample of roughness profiles for all three configurations are presented in Figure 4. The $R_N = 15$ mm nosetip exhibits the highest amplitude surface features among the three geometries tested, with peak-to-valley roughness on the order of 30 μm and a regular periodic peak spacing of 230 μm. The periodic pattern is observed in the other nosetips and is a result of the machine tool making cyclical passes. The $R_N = 20$ mm surface has significantly less amplitude in the roughness profiles compared to the $R_N = 15$ mm case. The peak-to-valley variation is on the order of 8 μm and the peak spacing is 145 μm. The largest nose radius, $R_N = 25$ mm, has very similar roughness to that of the $R_N = 20$ mm. Peak-to-valley is also near 8 μm and peak spacing is 110 μm. This uniformity reflects the reproducibility of the machining process. It seems that when the $R_N = 15$ mm nose tip was re-machined later, a different combination of tool and machine speed produced a significantly rougher surface finish.

3.3. Transition Reversal Comparison

Stetson [1] proposed a correlation for transition reversal based on nose tip surface roughness and boundary layer properties evaluated at the sonic point on the nose. In the present study, these boundary layer properties were obtained using a laminar solution generated with Eilmer4 [23], assuming a constant wall temperature of 298 K. The boundary layer edge was defined as the wall-normal location at which the total enthalpy reaches 99.5% of the freestream value, following the methodology outlined by Reda [24] and Edquist et al. [25]. The boundary layer edge was used to determine the sonic point, from which boundary layer momentum thickness θ was determined. The measured surface roughness values, reported as root-mean-squared (rms) or Rq, along with the corresponding boundary layer conditions, are summarised in Table 2.

Figure 5 compares the present experimental data with the transition reversal correlation for slender cone geometries proposed by Stetson [1]. The solid line corresponds to the PANT/Demetriades correlation [26, 27], developed for predicting boundary-layer transition onset due to roughness on nosetips and is widely validated across multiple datasets.

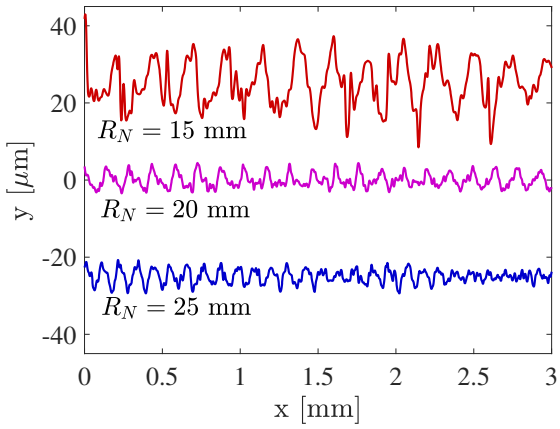

Fig. 4. Streamwise surface roughness profiles. Profiles are offset from one another by 25 μm for clarity.

Table 2. Results of surface roughness scans and estimation of sonic point boundary layer properties

Condition (-)	Nosetip (mm)	k (rms) (μm)	T_e (K)	θ (μm)	Re_θ (-)
E	15	4.9-6.9	364	8.1	81.7
F	20	1.7-1.9	378	9.9	98.6
G	25	1.6-1.8	376	10.3	104.9

Stetson's data (see Figure 10 from [1]), plotted as black markers is also discussed in detail by Schneider [3]. Based on his results, Stetson proposed that transition reversal would occur at 40% of the Reynolds numbers of the PANT & Demetriades nosetip transition correlation. The transition reversal mechanism remains unknown; thus it is not clear whether the parameters in Figure 5 capture all the relevant dynamics. Nevertheless, this remains the only published correlation for transition reversal and therefore it is a good starting place for contextualizing our results.

The present results, indicated by red markers, show transition reversal at approximately 36% of the PANT/Demetriades Reynolds number, slightly below Stetson's data. Although closely aligned, the datasets differ in the origin of surface roughness. All nosetips in this study were machined identically without subsequent treatment, resulting in azimuthally uniform, periodic surface features such as directional tool marks. These manufacturing-induced roughness patterns contrast with the randomised and evenly distributed roughness of sandblasted surfaces from Stetson's work. Despite similar amplitudes, the spatial arrangement and directional bias of the machined roughness may modify the growth of instabilities. In addition, the precise roughness spectrum of Stetson's nosetips remains unquantified, which may contribute to the modest discrepancy between results. It is also notable that Figure 5 does not account for tunnel noise which will differ significantly between facilities.

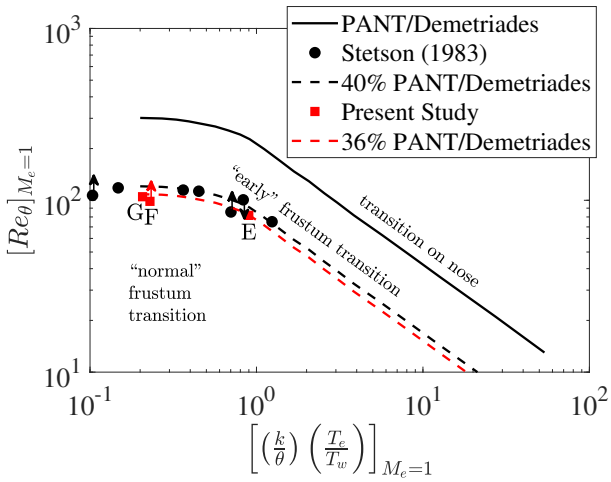

Fig. 5. Stetson's transition reversal correlation.

3.4. Spectral Characterisation of Boundary-Layer Disturbances

A series of schlieren images for conditions A-D are previously presented in [12]. In the present work, we investigated the temporal and spectral characteristics of the surface-adjacent disturbances observed in the schlieren images using spectral proper orthogonal decomposition (SPOD) [28] and continuous wavelet transform (CWT) analysis. These methods are complementary: SPOD identifies the energetically dominant coherent structures in the flow, while CWT captures the transient frequency content at a fixed spatial location. Together, they allow for a more comprehensive interpretation of the spatio-temporal dynamics underlying the observed transitional boundary layers.

An example frame sequence for condition A is presented in Figure 6. The time between frames is 40 μs and the dots indicate the pixels where CWT were applied. The boundary layer, represented with lighter pixels, is approximately 2 mm thick for this condition. A continuous wavelet scalogram, shown in Figure 7, which represents pixels at the mid-span of the field of view, shows that a persistent energy band between 20 and 50 kHz is observed at a wall normal height of 2 mm between frames 2 and 4 of the image sequence. These features coincide with the presence of coherent elongated features in the images and reinforce the interpretation of these structures as low-frequency, spatially extended wave packets or striations.

The SPOD spectrum in Figure 8 shows a modest peak in modal energy at 21.5 kHz and a harmonic peak at 43 kHz, which contrasts with the stronger and higher frequency peaks typically associated with second-mode instabilities. This

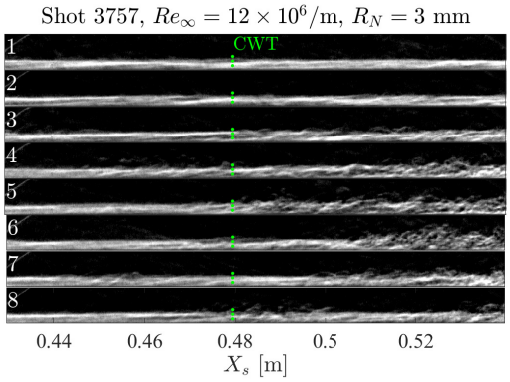

Fig. 6. Schlieren frame sequence for condition A.

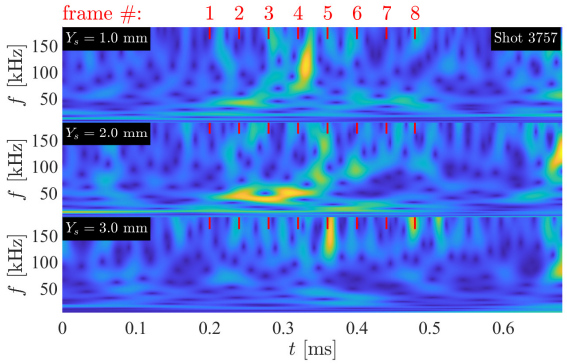

Fig. 7. CWT for condition A.

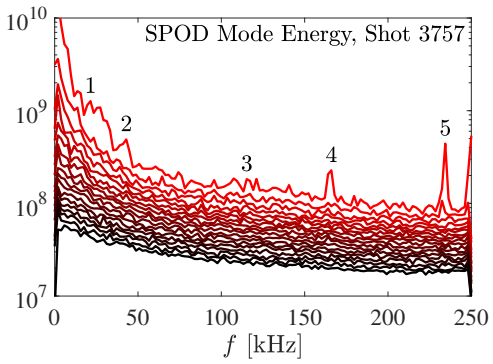

Fig. 8. SPOD spectrum for condition A.

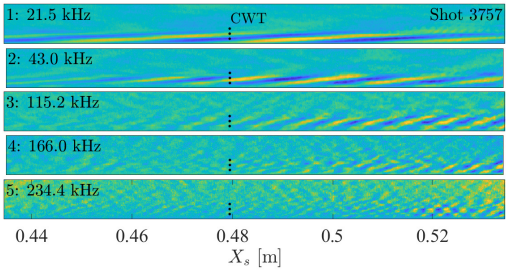

Fig. 9. SPOD structures for condition A.

mode exhibits strong coherence and is associated with the near-wall, nearly-surface-parallel structures visualised in the schlieren sequence. The corresponding spatial structures in frames 1 and 2 of Figure 9 confirms that these modes reside just above the edge of the boundary layer and maintain lateral coherence.

A secondary high-frequency band in the range of 100–130 kHz appears in the CWT in frame 4, localised near a height of 1 mm. This is followed in frame 5 by the emergence of a higher-frequency peak above 150 kHz at a wall normal height of 3 mm. This temporal and spatial shift in energy suggests a transient instability event or a possible breakdown of the initial disturbance. Notably, the SPOD spectrum exhibits no clear peak at 115 kHz, indicating that this phenomenon is a temporally localised event. In contrast, there is a strong energy peak at 166 kHz. This frequency is near the expected range of Mack's 2nd mode [29].

Similar features, frequencies, and structures are observed in conditions B, C, and D. In general, broad peaks between 20–100 kHz are observed in the SPOD spectrum, which are associated with the elongated structures. Peaks above 130 kHz dimmish rapidly with increasing bluntness Reynolds number. For conditions E and G, no spectral features are identified, rather, periodic turbulent spots are observed indicating that the boundary layer has transitioned far upstream of the schlieren field of view.

4. CONCLUSIONS

This study builds on previous work [12, 20] by incorporating surface roughness characterisation and spectral analysis to investigate boundary layer transition reversal on a 7-degree half-angle cone in Mach 6 flow. Transition reversal was observed for 15 mm and 25 mm nosetips, but not for 20 mm, correlated with differences in surface finish. Profilometry showed that the 15 mm tip had significantly higher amplitude roughness compared to the other tips.

The boundary layer properties at the sonic point were estimated using laminar simulations, allowing comparison with Stetson's correlation. Boundary layer transition reversal occurred at approximately 36% of the PANT/Demetriades [27] transition criterion, slightly below Stetson's data at 40% [1]. The discrepancy could be explained by an insufficient number of data points for both experiments or because the parameters in Figure 5 do not fully capture the transition reversal mechanism. Additional parameters could include more detailed descriptors of nosetip roughness, boundary layer properties, or facility noise.

Spectral analysis using SPOD and CWT revealed coherent low-frequency disturbances (20–50 kHz) and higher-frequency features (up to 166 kHz) in the boundary and entropy layer for Reynolds numbers just below transition reversal conditions. These decreased in energy with increasing bluntness Reynolds number; at the highest values, no spectral features were seen, indicating an upstream transition.

Further investigation with more variations in roughness and comparison across different facilities would be good follow-on work. Future work should also investigate the boundary and entropy layer just downstream of the nose under reversal conditions. The challenge is finding a measurement technique with sufficient spatial resolution and sensitivity to resolve features in the extremely thin (< 100 μm) boundary layers at these conditions.

5. REFERENCES

[1] Kenneth Stetson, "Nosetip bluntness effects on cone frustum boundary layer transition in hypersonic flow," in *16th Fluid and Plasmadynamics Conference*, 1983, p. 1763.

[2] Eric C Marineau, George C Moraru, Daniel R Lewis, Joseph D Norris, John F Lafferty, Ross M Wagnild, and Justin A Smith, "Mach 10 boundary layer transition experiments on sharp and blunted cones," in *19th AIAA International Space Planes and Hypersonic Systems and Technologies Conference*, 2014, p. 3108.

[3] S. P. Schneider, "Hypersonic laminar–turbulent transition on circular cones and scramjet forebodies," *Progress in Aerospace Sciences*, vol. 40, no. 1, pp. 1–50, 2004.

[4] E. R. Van Driest, "The problem of aerodynamic heating," *Aeronautical Engineering Review*, vol. 14, pp. 26–41, 1956.

[5] E. R. G. Eckert, "Survey of boundary layer heat transfer at high velocities and high temperatures," Tech. Rep. WADC-TR-59-624, University of Minnesota, Heat Transfer Lab, 1960.

[6] J. S. Jewell and R. L. Kimmel, "Boundary-layer stability analysis for stetson's mach 6 blunt-cone experiments," *Journal of Spacecraft and Rockets*, vol. 54, no. 1, pp. 258–265, 2017.

[7] P. Paredes, M. M. Choudhari, and F. Li, "Mechanism for frustum transition over blunt cones at hypersonic speeds," *Journal of Fluid Mechanics*, vol. 894, pp. A22, 2020.

[8] Alexandre R. Berger and Matthew P. Borg, "Co-linear FLDI/Schlieren and Surface Pressure Measurements of Bluntness Induced Elongated Structures in Hypersonic Flow," in *AIAA Scitech 2023 Forum*, National Harbor, MD & Online, Jan. 2023, American Institute of Aeronautics and Astronautics.

[9] Andrew B. Hartman, Christoph Hader, and Hermann F. Fasel, "Nonlinear transition mechanism on a blunt cone at Mach 6: oblique breakdown," *Journal of Fluid Mechanics*, vol. 915, pp. R2, May 2021.

[10] Richard E. Kennedy, Joseph S. Jewell, Pedro Paredes, and Stuart J. Laurence, "Characterization of instability mechanisms on sharp and blunt slender cones at Mach 6," *Journal of Fluid Mechanics*, vol. 936, pp. A39, Apr. 2022, Publisher: Cambridge University Press.

[11] Guillaume Grossir, Fabio Pinna, and Olivier Chazot, "Influence of Nose-Tip Bluntness on Conical Boundary-Layer Instabilities at Mach 10," *AIAA Journal*, vol. 57, no. 9, pp. 3859–3873, Sept. 2019, Publisher: American Institute of Aeronautics and Astronautics.

[12] A. P. Ceruzzi, L. M. Le Page, L. P. McQuellin, W. Condren, and M. McGilvray, "Observations of boundary layer transition reversal on a blunt cone in hypersonic flow," *AIAA SciTech Forum*, 2025.

[13] S. J. Laurence, A. Wagner, and K. Hannemann, "Experimental study of second-mode instability growth and breakdown in a hypersonic boundary layer using high-speed schlieren visualization," *Journal of Fluid Mechanics*, vol. 797, pp. 471–503, 2016.

[14] Matthew McGilvray, Luke J. Doherty, Andrew J. Neely, Robert Pearce, and Peter Ireland, "The Oxford High Density Tunnel," in *20th AIAA International Space Planes and Hypersonic Systems and Technologies Conference*. July 2015, American Institute of Aeronautics and Astronautics.

[15] S. Wylie, L. Doherty, and M. McGilvray, "Commissioning of the oxford high density tunnel (hdt) for boundary layer instability measurements at mach 7," in *2018 Fluid Dynamics Conference*. AIAA, 2018.

[16] Jack Hillyer, Luke Doherty, Christopher Hambidge, and Matthew McGilvray, "Extension of test time in Ludwieg tunnels," in *International Conference on Flight Vehicles, Aerothermodynamics and Re-entry Missions & Engineering*, Heilbronn, Germany, June 2022, p. 11.

[17] Tobias Hermann, Matthew McGilvray, Christopher Hambidge, and Luke Doherty, "Total temperature measurements in the oxford high density tunnel," in *International Conference on Flight Vehicles, Aerothermodynamics and Re-entry Missions & Engineering*, Monopoli, Italy, Oct. 2019.

[18] F. G. Keyes, "A summary of viscosity and heat-conduction data for he, a, h2, o2, n2, co, co2, h2o, and air," *Transactions of the American Society of Mechanical Engineers*, vol. 73, no. 5, pp. 589–595, 1951.

[19] S. Wylie, *Hypersonic boundary layer instability measurements at low and high angles of attack*, Ph.D. thesis, University of Oxford, 2020.

[20] Andrew Ceruzzi, Laurent M Le Page, Philipp Kerth, Benjamin A Williams, and Matthew McGilvray, "Simultaneous measurements of freestream disturbances, boundary layer instabilities, and transition location on sharp and blunt cones in hypersonic flow," in *AIAA SciTech 2024 Forum*, 2024, p. 2187.

[21] Lester Lees, "Laminar heat transfer over blunt-nosed bodies at hypersonic flight speeds," *Journal of Jet Propulsion*, vol. 26, no. 4, pp. 259–269, 1956.

[22] B. J. Griffith and Clark H. Lewis, "A study of laminar heat transfer to spherically blunted cones and hemisphere-cylinders at hypersonic conditions," Tech. Rep., Defense Technical Information Center, Fort Belvoir, VA, June 1963.

[23] Nicholas N. Gibbons, Kyle A. Damm, Peter A. Jacobs, and Rowan J. Gollan, "Eilmer: An open-source multi-physics hypersonic flow solver," *Computer Physics Communications*, vol. 282, pp. 108551, 2023.

[24] Daniel C Reda, "Boundary-layer transition experiments on sharp, slender cones in supersonic free flight," *AIAA Journal*, vol. 17, no. 8, pp. 803–810, 1979.

[25] Karl T Edquist, Derek S Liechty, Brian R Hollis, Stephen J Alter, and Mark P Loomis, "Aeroheating environments for a mars smart lander," *Journal of Spacecraft and Rockets*, vol. 43, no. 2, pp. 330–339, 2006.

[26] A.D. Anderson, "Passive nosetip technology (pant) program, interim report, volume x, appendix a: Boundary layer transition on nosetips with rough surfaces," Tech. Rep. SAMSO-TR-74-86, 1975.

[27] A. Demetriades, "Nosetip transition experimentation program, final report, vol ii," Tech. Rep. SAMSO-TR-76-120, July 1977.

[28] Oliver T. Schmidt, Aaron Towne, Georgios Rigas, Tim Colonius, and Guillaume A. Brès, "Spectral analysis of jet turbulence," *Journal of Fluid Mechanics*, vol. 855, pp. 953–982, Nov. 2018.

[29] Leslie M. Mack, "Linear Stability Theory and the Problem of Supersonic Boundary- Layer Transition," *AIAA Journal*, vol. 13, no. 3, pp. 278–289, Mar. 1975.